Electrostatic assist of liquid transfer between plates and cavities

Chung-Hsuan Huang,[1] Marcio S. Carvalho,[2] and Satish Kumar[1,*]
[1]*Department of Chemical Engineering and Materials Science, University of Minnesota, Minneapolis, Minnesota 55455, USA*
[2]*Department of Mechanical Engineering, Pontifícia Universidade Católica do Rio de Janeiro, Rio de Janeiro, RJ 22451-900, Brazil*

(Received 13 September 2018; published 16 April 2019)

Roll-to-roll printing processes require formation and stretching of a liquid bridge to transfer liquid from one surface to another. Since inadequate liquid transfer can produce defects that are detrimental to printed products, electric fields are sometimes applied to enhance transfer, a method known as electrostatic assist (ESA). Because the physical mechanisms underlying ESA are not well-understood, we examine here the influence of electric fields on liquid transfer in two model geometries, both of which involve liquid bridges with moving contact lines. The bridges are axisymmetric and confined between two electrodes, one of which is flat and moves vertically upward, and the other which either is flat or has a cavity and is stationary. An electric field is applied in the axial direction, both perfect and leaky dielectric liquids are considered, and the governing equations are solved with the Galerkin finite-element method. For liquid transfer between two flat plates, application of an electric field stabilizes the liquid bridge. This allows more time for the contact line to retract on the less wettable surface and leads to an increase in liquid transfer to the more wettable surface. Tangential stresses due to surface charge can significantly enhance liquid transfer, even to the less wettable surface if the tangential stresses point toward that surface. For liquid transfer between a flat plate and a cavity, the electric field increases the pressure gradient near the contact line on the cavity wall, causing the contact line to slip and more liquid to be transferred from the cavity. Notably, the effect is more pronounced for a deep cavity, resulting in a larger percentage of liquid transferred compared to a shallow cavity. In contrast to the case of liquid transfer between two flat plates, surface charge does not have as significant an influence on liquid transfer due to the way the cavity and electric field modify the interface shape near the contact line. The results of this work illustrate the physical mechanisms through which electric fields can improve liquid transfer, and they provide guidance for optimizing ESA in industrial printing processes.

DOI: 10.1103/PhysRevFluids.4.044005

I. INTRODUCTION

A. Motivation

Printing processes have been widely used to make newspapers and books, and they are increasingly being applied to fabricate electronic devices such as transistors [1–3], solar cells [4], and radiofrequency identification tags [5,6]. In these printing processes, functional inks are deposited onto flexible substrates made of materials such as plastic [7,8] or paper [9]. The flexible substrates are first unwrapped from a cylindrical roll and then wound up onto another cylindrical

*kumar030@umn.edu

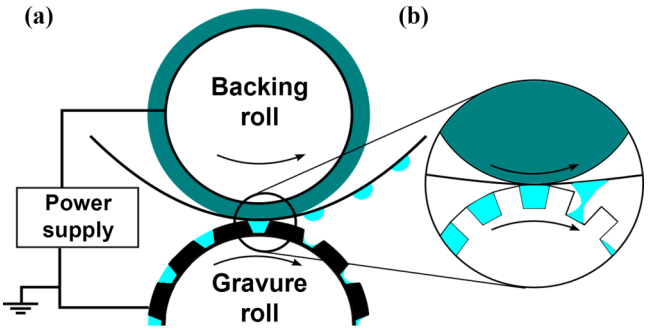

FIG. 1. (a) Schematic of a gravure printing process with electrostatic assist (ESA). Ink is transferred from a cavity to a substrate, sometimes with the help of an electrostatic potential difference. (b) Schematic of a stretching liquid bridge.

roll after printing and drying. Such roll-to-roll printing techniques have the potential to significantly reduce production costs and material waste [10] while still having high throughput ($\sim$1 m/s) [3,11].

A printing process of particular interest for electronics-related applications is gravure printing (Fig. 1) [12]. The gravure roll contains a pattern of pixelated micron-scale cavities on its surface. After the cavities are filled with printing ink (often from a pan into which the gravure roll enters and then leaves), ink is transferred from the cavities to a substrate (supported by a backing roll). Gravure has the potential to create patterns having length scales of 10 μm or less [12].

For printed electronics, insufficient ink transfer from the cavities could lead to broken circuits and failure of electronic devices. It has long been known that application of an electric field between the gravure roll and the substrate can help improve ink transfer, a technique known as electrostatic assist (ESA) (Fig. 1) [13–16]. However, the physical mechanisms underlying ESA remain poorly understood. A better understanding of these mechanisms would allow for more systematic design of ESA systems, which in turn would greatly help in reducing printing defects. The objective of this paper is to address this issue by examining the influence of electric fields on liquid transfer in two model geometries.

Gravure printing processes involve the formation of a liquid bridge when ink transfers from a cavity to the substrate (Fig. 1). During liquid transfer, the liquid bridge is, in general, subject to extensional, shear, and rotational motions [17,18]. Here, we consider the important limiting case of extensional motion where the liquid bridge is stretched between a vertically moving flat plate and a stationary (i) flat plate or (ii) cavity. Schematics of the two model geometries are shown in Fig. 2. A constant electrostatic potential is applied to the top surface, while the bottom surface remains grounded. The contact lines (where the air, liquid, and solid intersect) may slip along each solid surface. We seek to determine how the electric field influences the dependence of liquid transfer on surface wettability and the geometry of the bottom surface.

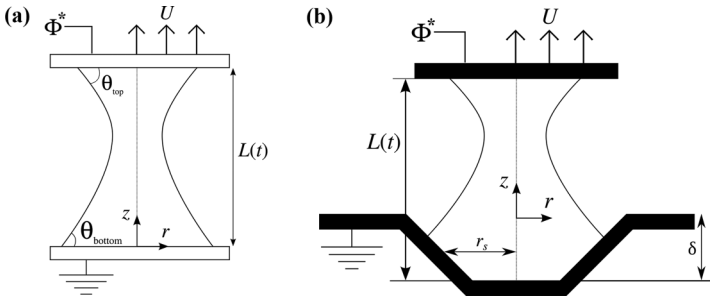

FIG. 2. Schematic of model geometries considered in this work. A liquid bridge between (a) two flat surfaces and (b) a flat surface and a cavity. The cavity bottom is located at $z = 0$.

B. Summary key findings from recent previous work

There have been a number of recent experimental [19–21] and theoretical [11,17,22–25] studies on liquid transfer between two flat plates in the absence of an electric field. We provide here a summary of the key findings.

For liquid transfer in printing processes, inertial and gravitational forces are often negligible relative to surface-tension and viscous forces due to the small length scales involved. Thus, the key parameter characterizing liquid transfer is the capillary number $\mathrm{Ca} = \mu U/\gamma$, the ratio of viscous to surface-tension forces. Here, μ is the liquid viscosity, U is the stretching speed, and γ is the liquid surface tension. When Ca is less than $\sim$0.01, liquid transfer is dominated by the wettability of the surfaces [19,24]. In this regime, the deformation of the liquid bridge is strongly coupled to contact-line motion. When Ca is $\sim$1, the stronger viscous forces tend to hinder contact-line movement and make wettability less important. As a result, only about 50% of the liquid is transferred from one surface to the other for a large range of wettability differences [20,24].

There have also been a number of recent experimental [26] and theoretical [22,23,25,27–29] studies on liquid transfer between a flat plate and a cavity in the absence of an electric field. In general, it is found that the amount of liquid transferred from the cavity is considerably less than 50%, even in the absence of a wettability difference between the cavity and the flat plate. This occurs because of an apparent pinning of the contact line on the inclined walls of the cavity (i.e., the contact line moves so slowly that it appears to be pinned) [22,26]. Increasing Ca tends to increase the amount of liquid transferred because the stronger viscous forces reduce the slippage of the contact line on the flat plate [22]. However, it does not get above 50%.

The above results suggest that liquid transfer at high printing speeds is not influenced by wettability differences, and that transferring liquid from cavities is considerably more difficult than transferring liquid from a flat surface. As mentioned in Sec. I A, one way to overcome these limitations is to apply an electric field. Although there is previous work examining the influence of electric fields on liquid bridges that have pinned contact lines and are not being stretched [30–33], very little work has been done to examine the fundamentals of stretching liquid bridges with moving contact lines in the presence of an electric field.

To address this knowledge gap, Huang and Kumar [34] developed a one-dimensional (1D) slender-jet model of stretching liquid bridges with moving contact lines in the presence of an electric field. The considered both perfect dielectric and leaky dielectric liquids. They found that the electric field modifies the pressure differences inside the liquid bridge, and as a consequence, it drives liquid toward the more wettable surface. For leaky dielectrics, charge can accumulate the liquid-air interface and further enhance liquid transfer, even to the less wettable surface. Thus, at high printing speeds ($\mathrm{Ca} \sim 1$), application of an electric field can allow one to overcome the 50% limit on liquid transfer.

To complement their modeling work, Huang and Kumar [34] also performed a limited number of flow visualization experiments. These showed that application of an electric field modifies the shape of the liquid bridge and can cause depinning of the contact line (whereas it would remain pinned in the absence of the electric field). For the pair of surfaces considered by Huang and Kumar [34], measured values of the amount of liquid transferred are in good agreement with predictions of the 1D slender-jet model for perfect dielectrics. Because both Ca and the ratio of electrostatic to surface-tension forces in those experiments are relatively small, predictions from the 1D model might be expected to agree well with experiments [24].

C. Overview of the present paper

Although the 1D slender-jet model is computationally efficient, it tends to overestimate contact-line motion, as shown in our previous work on stretching liquid bridges in the absence of electric fields [24]. While it sometimes yields predictions that agree well with experiments [24,34], an important open issue is how well predictions of the 1D model compare to those from a 2D axisymmetric model over a wide range of wettability differences in the presence of an electric

TABLE I. Order-of-magnitude values of key dimensional parameters.

Parameter	Typical values
Bridge radius R and bridge length L (mm)	10^{-3}–1
Liquid viscosity μ (cP)	1–10^{2}
Surface tension γ (mN/m)	10^{1}–10^{2}
Stretching speed U (mm/s)	1–10^{2}
Voltage V (V)	10^{2}–10^{4}
Conductivity K (S/m)	10^{-12}–10^{-6}
Contact-angle difference $\Delta\theta_r = \theta_{\text{bottom}} - \theta_{\text{top}}$ (deg)	-20°–20°

field. Moreover, liquid transfer from a cavity cannot be described by a 1D model since the cavity geometry varies in the radial direction, making this an inherently 2D problem. Thus, in the present work we perform 2D calculations to advance a fundamental understanding of how electric fields influence liquid transfer in the two model geometries shown in Fig. 2.

The mathematical model and computational scheme used in this work are presented in Sec. II. In Sec. III, results are presented and discussed for liquid transfer between two flat plates. Both perfect dielectric and leaky dielectric liquids are considered, and predictions from the 2D model are compared to those from the 1D model of our previous work [34]. In Sec. IV, liquid transfer from a cavity is considered, including an examination of the influence of cavity depth. Conclusions are summarized in Sec. V.

II. PROBLEM FORMULATION

Figure 2 shows the model geometries used in this work. We consider axisymmetric bridges of Newtonian liquids with constant density ρ, surface tension γ, viscosity μ, relative permittivity ϵ, and conductivity K confined between two electrodes. The top electrode is a flat horizontal plate moved vertically with a constant velocity U in the z-direction, and it has a fixed electrostatic potential ϕ^*. The bottom electrode is stationary and grounded. It can either be flat and horizontal [Fig. 2(a)] or have the shape of a trapezoidal cavity [Fig. 2(b)].

The contact angle on the top electrode is θ_{top}, and that on the bottom electrode is θ_{bottom}. These contact angles may be a function of contact-line speed [35,36], but we consider here the important limiting case in which they are constant. We neglect any flow in the air outside the bridge. Table I lists order-of-magnitude values of key dimensional parameters.

Both perfect and leaky dielectric liquids are considered [37–39]. Perfect dielectrics are nonconductive but polarizable. Leaky dielectrics are also polarizable, but a finite conductivity allows charge to accumulate at the liquid-air interface when an electric field is present (charge is assumed to be negligible in the bulk). Thus, the electric field can act on both the polarized charge and the interfacial charge in leaky dielectrics. The air phase is assumed to be a perfect dielectric with a relative permittivity of unity.

A. Governing equations

In the equations below, length is scaled by a characteristic initial bridge radius R (e.g., the radius corresponding to the narrowest point of the initial bridge shape), velocity by the constant stretching speed U, time by R/U, pressure by $\mu U/R$, electrostatic potential by ϕ^*, electric field by $E^* = \phi^*/L(0)$, where $L(0)$ is a characteristic initial bridge length, and charge density by $\epsilon_o E^*$, where ϵ_o is the free-space permittivity.

The electric field in each phase is given by $\mathbf{E}_i = -\nabla\phi_i$, where the electrostatic potentials ϕ_i are governed by Laplace's equation,

$$\nabla^2\phi_i = 0, \tag{1}$$

TABLE II. Dimensionless problem parameters. The ranges of values encompass both laboratory experiments and industrial practice.

Parameter	Definition	Physical meaning	Value
Bo	$\rho g R^2/\gamma$	$\frac{\text{Gravitational forces}}{\text{Surface-tension forces}}$	10^{-7}–1
Re	$\rho U R/\mu$	$\frac{\text{Inertial forces}}{\text{Viscous forces}}$	10^{-5}–10^{2}
Ca	$\mu U/\gamma$	$\frac{\text{Viscous forces}}{\text{Surface-tension forces}}$	10^{-5}–1
χ	$RE_o^2\epsilon_o/\mu U$	$\frac{\text{Electrostatic forces}}{\text{Viscous forces}}$	10^{-5}–10^{11}
Ca_E	$RE_o^2\epsilon_o/\gamma$	$\frac{\text{Electrostatic forces}}{\text{Surface-tension forces}}$	10^{-10}–10^{11}
ϵ		Relative permittivity	1–10^{1}
K^*	$(R/U)/(\epsilon_o/K)$	$\frac{\text{Time scale for stretching}}{\text{Characteristic time for electric phenomena}}$	10^{-6}–10^{5}
Λ	$L(0)/2R$	$\frac{\text{Initial bridge length}}{\text{Initial bridge diameter}}$	1

with $i = 1$ for liquid and $i = 2$ for air. The boundary conditions at the top and bottom electrode are

$$\phi_i = \begin{cases} 0 & \text{for } z = 0, \\ 1 & \text{for } z = L(t). \end{cases} \tag{2}$$

For the cavity, the condition $\phi_i = 0$ is applied on the cavity bottom ($z = 0$) as well as the cavity walls.

At the liquid-air interface, the surface charge density q is equal to the jump in the normal component of the electric field [39],

$$q = \| \epsilon_i \mathbf{E}_i \| \cdot \mathbf{n}, \tag{3}$$

where ϵ_i is the relative permittivity of each phase, $\mathbf{n}$ is the outward unit normal vector pointing into the air, and $\| \cdots \|$ is the jump operator, which denotes the quantities in the air phase minus those in the liquid phase. Note that we set $\epsilon_1 = \epsilon$ and $\epsilon_2 = 1$. The tangential components of the electric field are continuous at the liquid-air interface,

$$\| \mathbf{E}_i \| \cdot \mathbf{t} = 0, \tag{4}$$

where $\mathbf{t}$ is the unit tangent vector to the liquid-air interface.

The charge at the liquid-air interface is governed by the conservation equation

$$\frac{\partial q}{\partial t} + \mathbf{v} \cdot \nabla_s q = q\mathbf{n} \cdot (\mathbf{n} \cdot \nabla)\mathbf{v} + \| -K^* \mathbf{E}_i \| \cdot \mathbf{n} + \frac{1}{\text{Pe}} \nabla_s^2 q, \tag{5}$$

where $\mathbf{v}$ is the velocity vector, $\nabla_s = (\mathbf{I} - \mathbf{nn}) \cdot \nabla$ is the surface gradient operator, $K^* = RK/U\epsilon_o$ is the dimensionless conductivity, and $\text{Pe} = RU/D_s$ is the Peclet number, with D_s being the surface-charge diffusion coefficient. The last term corresponds to charge diffusion along the interface and is usually neglected [39]. However, we keep this term to resolve large charge gradients that form near the contact lines [40]. No-flux conditions are applied to the charge at each solid surface.

With the scales mentioned above, we can define a Reynolds number $\text{Re} = \rho U R/\mu$, Bond number $\text{Bo} = \rho g R^2/\gamma$, and electroviscous number $\chi = RE^2\ \epsilon_o/\mu U$, where g is the acceleration due to gravity. The physical meaning and typical values of these and other dimensionless parameters are listed in Table II. We choose to focus on the regime where Bo and Re are small so that gravitational and inertial forces can be neglected, and thus we set $\text{Bo} = \text{Re} = 0$.

The velocity and pressure in each phase are denoted as $\mathbf{v}_i$ and P_i. Because we neglect the dynamics of the air phase, we set $\mathbf{v}_2 = \mathbf{0}$ and $P_2 = 0$, and let $\mathbf{v}_1 = \mathbf{v}$ and $P_1 = P$. The mass and momentum conservation equations for the liquid are

$$\nabla \cdot \mathbf{v} = 0, \tag{6}$$

$$-\nabla P + \nabla^2 \mathbf{v} = \mathbf{0}. \tag{7}$$

The dimensionless Maxwell stress tensor is $\boldsymbol{\sigma}_i^M = \epsilon_i \mathbf{E}_i\mathbf{E}_i - \frac{1}{2}\epsilon_i \mathbf{E}_i \cdot \mathbf{E}_i \mathbf{I}$, with $\mathbf{I}$ being the identity tensor. [We have scaled $\boldsymbol{\sigma}_i^M$ by $\epsilon_o (E^*)^2$.] Because the divergence of the Maxwell stress tensor is zero for perfect and leaky dielectrics [39], it does not appear in Eq. (7). As a result, electrostatic and hydrodynamic phenomena are connected only through the normal and tangential stress balances [Eqs. (9) and (10)] at the liquid-air interface [41].

At the liquid-air interface, we impose the kinematic condition,

$$\mathbf{n} \cdot (\mathbf{v} - \dot{\mathbf{x}}) = 0, \tag{8}$$

where $\dot{\mathbf{x}}$ is the interface velocity. The normal stress balance is given by

$$\| \mathbf{n} \cdot \mathbf{T}_i \cdot \mathbf{n} \| = -\frac{\kappa}{\mathrm{Ca}}, \tag{9}$$

where $\mathbf{T}_i = -P_i \mathbf{I} + [\nabla \mathbf{v}_i + (\nabla \mathbf{v}_i)^T] + \chi \boldsymbol{\sigma}_i^M$ is the total stress tensor, Ca is the capillary number, and $\kappa = \nabla_s \cdot \mathbf{n}$ is the interface curvature. The tangential stress balance is

$$\| \mathbf{n} \cdot \mathbf{T}_i \cdot \mathbf{t} \| = 0. \tag{10}$$

The normal and tangential components of the Maxwell stress can be written as

$$\left\| \mathbf{n} \cdot \boldsymbol{\sigma}_i^M \cdot \mathbf{n} \right\| = \frac{\chi}{2} \, \| \epsilon_i (\mathbf{E}_i \cdot \mathbf{n})^2 - \epsilon_i (\mathbf{E}_i \cdot \mathbf{t})^2 \|, \tag{11}$$

$$\left\| \mathbf{n} \cdot \boldsymbol{\sigma}_i^M \cdot \mathbf{t} \right\| = q\chi (\mathbf{E}_i \cdot \mathbf{t}). \tag{12}$$

Note that the tangential component of the electric field is continuous at the liquid-air interface [Eq. (4)].

We apply the no-penetration and no-slip conditions at each solid surface,

$$\mathbf{n}_{\mathrm{wall}} \cdot \mathbf{v} = \begin{cases} 0 & \text{for } z = 0, \\ 1 & \text{for } z = L(t), \end{cases} \tag{13}$$

$$\mathbf{t}_{\mathrm{wall}} \cdot \mathbf{v} = \mathbf{0} \quad \text{at } z = 0, L(t), \tag{14}$$

where $\mathbf{n}_{\mathrm{wall}}$ is the unit normal vector pointing in the positive z-direction, $\mathbf{t}_{\mathrm{wall}}$ is the unit tangent vector pointing in the radial direction, and $L(t)$ is the location of the top plate. For the cavity, these conditions are applied on the cavity bottom ($z = 0$) as well as the cavity walls.

We apply symmetry boundary conditions at the bridge axis,

$$\mathbf{t}_{\mathrm{symm}} \cdot (\mathbf{n}_{\mathrm{symm}} \cdot \mathbf{T}) = 0, \tag{15}$$

$$\mathbf{n}_{\mathrm{symm}} \cdot \mathbf{v} = 0, \tag{16}$$

where $\mathbf{n}_{\mathrm{symm}}$ and $\mathbf{t}_{\mathrm{symm}}$ are the unit vectors normal and tangent to the symmetry line.

To deal with the dynamic contact line, we replace Eq. (14) with a Navier slip condition at each contact line, and we fix the contact angle instead of the contact-line position,

$$\mathbf{t}_{\mathrm{wall}} \cdot (\mathbf{n}_{\mathrm{wall}} \cdot \mathbf{T}) = \frac{1}{\beta} \mathbf{t}_{\mathrm{wall}} \cdot (\mathbf{v} - \mathbf{v}_{\mathrm{wall}}), \tag{17}$$

$$\mathbf{n}_{\mathrm{wall}} \cdot \mathbf{n} = \cos\theta, \tag{18}$$

where $\mathbf{n}_{\mathrm{wall}}$ (which points toward the liquid side) and $\mathbf{t}_{\mathrm{wall}}$ are unit normal and tangent vectors to each solid surface, β is a dimensionless slip coefficient, and $\mathbf{v}_{\mathrm{wall}}$ is the wall velocity. For all computations, the value of β is set to 10^{10} to produce a contact line with negligible shear stress [22–24], but the results are essentially independent of β down to a value of 0.1. Here, $\theta = \theta_{\mathrm{bottom}}$ at the bottom surface and $\theta = \theta_{\mathrm{top}}$ at the top surface. Note that we only impose Eqs. (17) and (18)

at the node located on the contact line, and the no-slip condition is applied on the rest of the solid surface, i.e., the slip length is less than the size of an element [22–24].

As shown in Fig. 2, we consider two model geometries. The cavity wall [Fig. 2(b)] is defined by a hyperbolic tangent function [22–24],

$$z = \frac{1}{2}\delta\left[1 + \tanh\left(\frac{r - r_s}{r_d}\right)\right], \tag{19}$$

where z and r are the axial and radial positions of the cavity wall, respectively, δ is the depth of the cavity, r_s represents the distance from the midpoint of the cavity wall to the symmetry axis, and r_d controls the slope of the cavity and the curvature of the corner. (Increasing the value of r_d increases the radius of curvature of the corner.)

In this work, we study the transfer ratio (mass fraction of liquid transferred to the top plate) as a function of the capillary number Ca and the electroviscous number χ (Table II). For leaky dielectrics, the dimensionless conductivity K^* and initial surface charge density also come into play.

B. Solution method

Equations (1)–(18) are solved using the Galerkin finite-element method [22–24,27] with elliptic mesh generation to track the moving interface. Biquadratic basis functions are used for the velocity, electrostatic potential, and mesh position, whereas linear discontinuous basis functions are used for the pressure. For the surface charge along the liquid-air interface, we use quadratic basis functions. A first-order backward Euler method is applied in the first two time steps to prevent abrupt oscillations. A second-order trapezoid rule with variable time-step size is then used to perform time integration [42].

For the simulations between two flat plates, the computational mesh typically involves 64 elements in the axial direction and 25 elements in the radial direction (15 and 10 elements in the liquid and air phases, respectively). For the simulations between a flat plate and a cavity, the computational mesh typically involves 48 elements in the axial direction and 40 elements in the radial direction (22 and 18 elements in the liquid and air phases, respectively). The mesh is refined near the liquid-air interface and contact lines.

When the liquid bridge nears breakup, a thin thread connecting a droplet on each solid surface is formed. Eventually, the elements in the thread become extremely deformed and elongated, causing the simulation to fail. At the end of the simulation, the narrowest bridge radius is roughly 0.1% of its initial radius. The overall bridge shape has primarily been determined at this point, so the transfer ratio will likely not vary significantly even if the bridge stretches further. After a simulation ends, we check whether the variation from the initial bridge volume is less than 0.1% to ensure mass conservation. If the change of volume is greater than 0.1%, we rerun the simulation with a refined mesh or time step.

III. RESULTS—FLAT PLATES

When a liquid bridge is stretched between two flat plates without an electric field, both theoretical and experimental results show that the transfer ratio (mass fraction of liquid transferred to the top plate) is mainly determined by the wettability difference between the two plates at low Ca (<0.01) [19,24]. When Ca is large enough (~ 1), the transfer ratio is about 50% and independent of the wettability difference [20,24]. In this section, we explore how electric fields influence liquid transfer when both plates are flat. The results presented here complement those obtained in our earlier work using a 1D slender-jet model [34].

The initial bridge shape is a cylinder with length $L(0)$ and radius R. In our prior work [22,24,25,34], we used a cylinder as the initial shape to focus on the influence of wettability differences at a given value of Ca. Although the initial bridge shape can significantly influence liquid

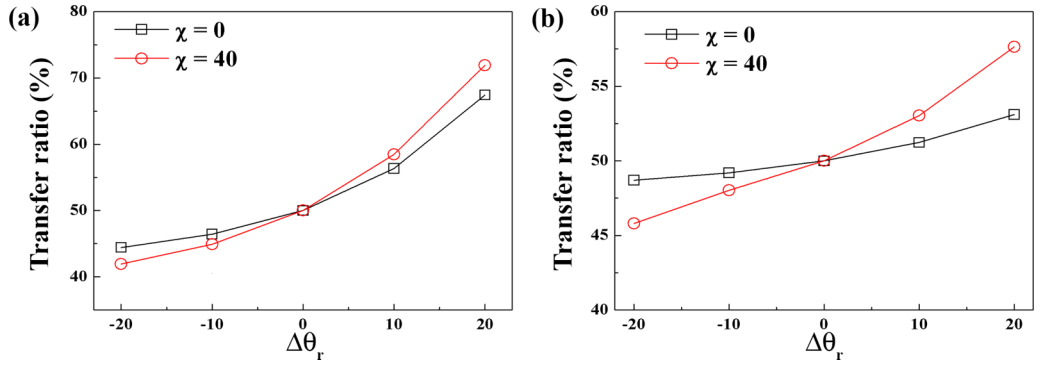

FIG. 3. Relationship between the transfer ratio and the wettability difference for different values of χ at (a) Ca = 0.1 and (b) Ca = 0.5. Here, $\theta_{\text{top}} = 60^\circ$, and θ_{bottom} varies from 40° to 80°. The wettability difference $\Delta\theta_r = \theta_{\text{bottom}} - \theta_{\text{top}}$.

transfer [24,34], we use a cylinder here since initial-shape effects have been studied previously [24,34], and we would now like to isolate the influence of electric fields. (In general, changing the initial shape of the bridge produces quantitative changes in the results but does not change the qualitative behavior [24,34].) For simplicity, we set $L(0) = 2R$ so that the aspect ratio is unity. The contact angles reach their prescribed values after the first time step, and the overall run time is much longer than this, so this "equilibration" step does not play an important role in the overall bridge dynamics.

The top contact angle θ_{top} is set to 60°, while the bottom contact angle θ_{bottom} ranges from 40° to 80°. The wettability difference $\Delta\theta_r = \theta_{\text{bottom}} - \theta_{\text{top}}$, so positive $\Delta\theta_r$ means that the bottom plate is less wettable than the top plate. We fix the value of ϵ to the representative value of 2.74 (silicone oil); increasing this will tend to enhance the effect of electric fields. Two values of the capillary number Ca (0.1 and 0.5) are considered, and the electroviscous number χ is set to 0 (no electric field) or 40.

A. Perfect dielectrics

1. Liquid transfer

We begin by examining transfer of a perfect dielectric liquid between two flat plates by setting $q = 0$ and $K^* = 0$. Figure 3(a) shows the relationship between the transfer ratio and the wettability difference $\Delta\theta_r$ at Ca = 0.1. When $\chi = 0$, the transfer ratio increases as $\Delta\theta_r$ increases. Because the bottom plate becomes less wettable as $\Delta\theta_r$ increases, more liquid is transferred to the top plate. When χ increases from 0 to 40, the transfer ratio increases when $\Delta\theta_r$ is positive. However, when $\Delta\theta_r$ is negative, the transfer ratio decreases when an electric field is present. These results indicate that electric fields enhance liquid transfer to the more wettable surface.

Figure 3(b) presents the transfer ratio as a function of $\Delta\theta_r$ at Ca = 0.5. When $\chi = 0$, the transfer ratio also increases as $\Delta\theta_r$ increases. However, the transfer ratios are 50% ± 3% for all values of $\Delta\theta_r$ since the viscous forces are stronger at higher Ca and reduce the influence of wettability differences. This represents a limit on how much liquid can be transferred at high printing speeds.

As can be seen in Fig. 3(b), the presence of the electric field enhances the influence of wettability differences when Ca = 0.5. This suggests that electric fields may be a useful tool for increasing liquid transfer at high printing speeds. Note that the electrocapillary number $\text{Ca}_E = \chi\text{Ca}$ provides a measure of the strength of electrostatic forces to surface-tension forces, and it is smaller for fixed χ at smaller Ca. Thus, the electric field does not influence the transfer ratio as much at lower Ca [Fig. 3(a)] compared to higher Ca [Fig. 3(b)].

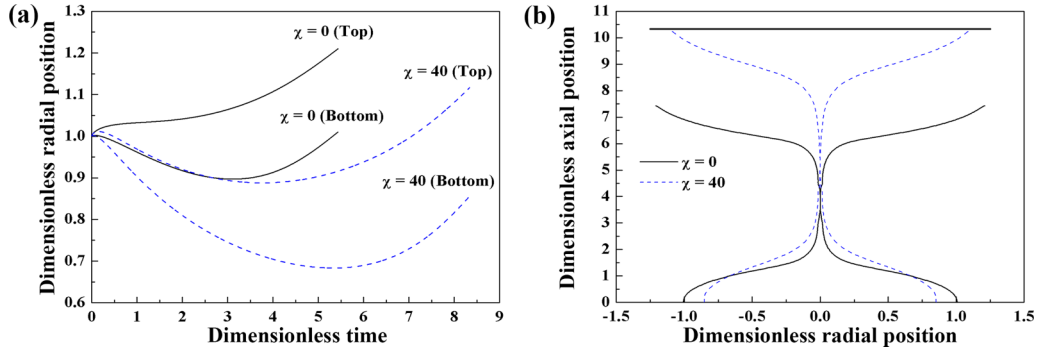

FIG. 4. (a) Time evolution of the contact line on the top and bottom plates for $\chi = 0$ (solid line) and 40 (dashed line). (b) Final bridge shapes for $\chi = 0$ (solid line) and 40 (dashed line). The bridge breakup times for $\chi = 0$ and 40 are 5.4 and 8.3, respectively. The values of the other parameters are Ca = 0.5, $\theta_{\text{top}} = 60^\circ$, $\theta_{\text{bottom}} = 80^\circ$, and $\Delta\theta_r = 20^\circ$.

Results from the 1D slender-jet model used in our previous work [34] show qualitatively similar behavior. However, the 1D model predicts much more liquid transfer compared to the 2D model. A more detailed comparison can be found in the Supplemental Material [43].

We now consider the case in which $\Delta\theta_r = 20^\circ$ and Ca = 0.5 to characterize contact-line motion and bridge shapes. Figure 4(a) shows the time evolution of contact-line positions. When $\chi = 0$, the top contact line simply expands in the radial direction, while the bottom contact line first retracts and then expands. However, when $\chi = 40$, both contact lines retract and then expand. Note that the bottom contact radius decreases faster than the top contact radius when $\chi = 40$ because the bottom surface is less wettable.

Figure 4(b) compares the final bridge shapes for $\chi = 0$ and 40. In Fig. 4(b), the difference between the top and bottom contact radii of the electrified bridge (0.26) is larger than that of the nonelectrified bridge (0.20) when the simulation ends. In addition, the electrified bridge breaks up at a longer length. These results suggest that the electric field stabilizes the liquid bridge and amplifies the influence of wettability differences, a feature we will discuss further in Sec. III A 2.

2. Physical mechanisms

For perfect dielectrics, the only way the electric field influences the liquid bridge is through the normal stress balance [Eq. (11)]. It is instructive to examine this boundary condition in the slender-jet limit, as it yields an expression for the liquid pressure [34],

$$P = \frac{\kappa}{\text{Ca}} - v_z - \chi \frac{\epsilon - 1}{2} E^2, \tag{20}$$

where E is the leading-order axial component of the electric field. The three terms on the right-hand side of Eq. (20) represent contributions from surface tension, viscous forces, and electrostatic forces, respectively. Note that the pressure in Eq. (20) only depends on the axial coordinate due to the slender-jet approximation. Because χ is always positive and ϵ is greater than 1, the electrostatic term in Eq. (20) is always negative. As a result, the electrostatic term lowers the pressure in the bridge.

We now plot pressure contours and bridge shapes predicted by the 2D model for the case in which Ca = 0.5 and $\Delta\theta_r = 20^\circ$ to gain insight into the observations of Sec. III A 1. The physical mechanisms we will discuss also hold at lower values of Ca. For convenience, we rotate the bridge 90° clockwise so the top (bottom) surface is on the right (left) in Fig. 5.

Figure 5(a) shows pressure contours when $\chi = 0$ at $t = 0.6$. The highest pressure is near the left (bottom) contact line, while the lowest pressure is near the right (top) contact line. Since liquid

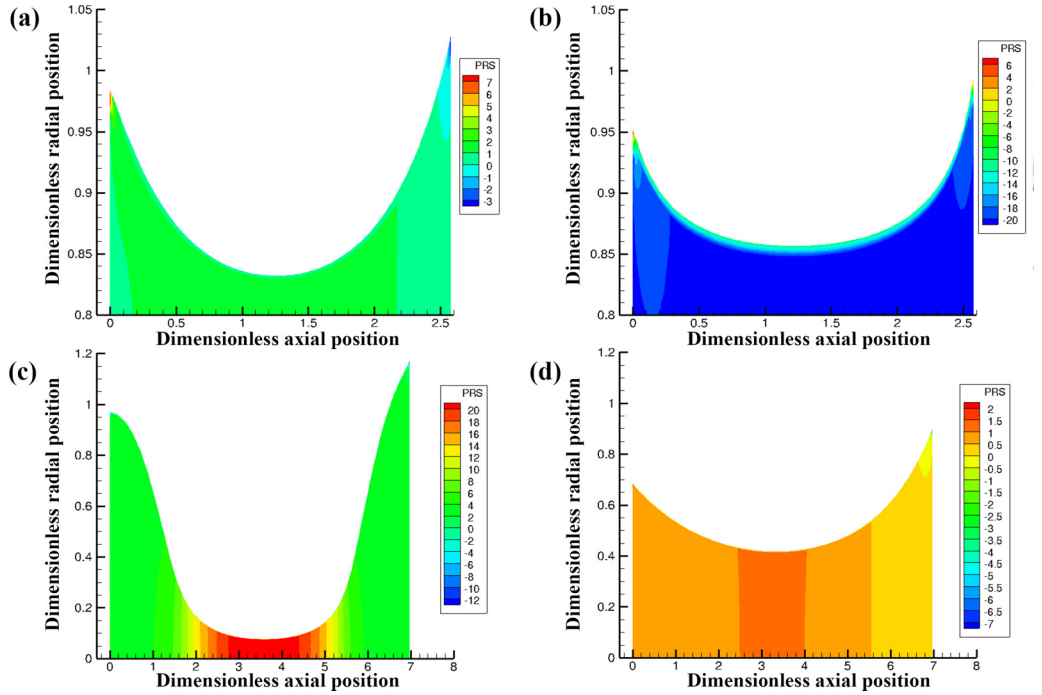

FIG. 5. Pressure contours and bridge shapes for the cases in which (a), (c) $\chi = 0$ and (b), (d) $\chi = 40$ at (a), (b) $t = 0.6$ and (c), (d) $t = 5$. The bridge breakup times for $\chi = 0$ and 40 are 5.4 and 8.3, respectively. The values of the other parameters are $\mathrm{Ca} = 0.5$, $\theta_{\mathrm{top}} = 60^\circ$, $\theta_{\mathrm{bottom}} = 80^\circ$, and $\Delta\theta_r = 20^\circ$.

flows from regions of higher pressure to lower pressure, the bottom contact radius decreases while the top contact radius increases [Fig. 4(a)].

Figure 5(b) shows pressure contours when $\chi = 40$ at $t = 0.6$. The pressure near both contact lines is larger than the pressure near the bridge center. This can be understood by noting that the axial component of the electric field is stronger near the bridge center than near the contact lines, as can be seen by examining the electrostatic potential contours in Fig. 6(a). According to Eq. (5), the electric field will lower the pressure the most near the bridge center. The resulting pressure

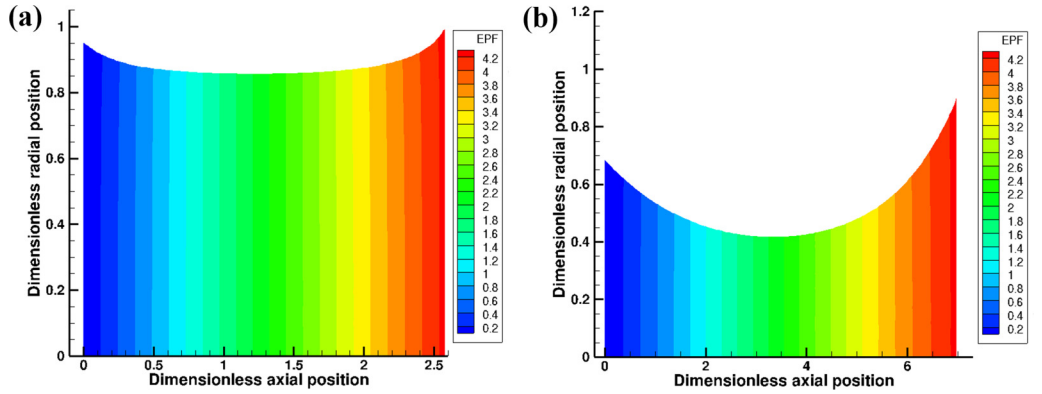

FIG. 6. Electrostatic potential contours and bridge shapes for the case in which $\chi = 40$ at (a) $t = 0.6$ and (b) $t = 5$. The values of the other parameters are $\mathrm{Ca} = 0.5$, $\theta_{\mathrm{top}} = 60^\circ$, $\theta_{\mathrm{bottom}} = 80^\circ$, and $\Delta\theta_r = 20^\circ$.

gradients cause both contact lines to retract. Because the left (bottom) surface is less wettable than the right (top) surface, the left contact line retracts faster than the right contact line [Fig. 4(a)]. The lower pressure in the bridge center when the electric field is present also implies that the bridge is stabilized by the electric field and should stretch longer before breaking up.

Figure 5(c) shows pressure contours when $\chi = 0$ at $t = 5$. Because this is close to the breakup time of $t = 5.4$, the highest pressure is near the bridge center. The resulting pressure gradients push liquid away from the bridge center toward each plate. As a consequence, the contact radii increase near the end of stretching [Fig. 4(a)].

Figure 5(d) shows pressure contours when $\chi = 40$ at $t = 5$. The pressure near the left (bottom) plate is larger compared to that near the right (top) plate, and the maximum pressure occurs near the bridge center. In addition, the radial component of the electric field becomes more pronounced (relative to the axial component) near the contact lines, as can be seen by examining the electrostatic potential contours in Fig. 6(b). Since the electrostatic potential at the top plate is a constant, the influence of electrostatic forces becomes weaker during stretching, and eventually the region of highest pressure occurs near the bridge center. As a consequence, both contact lines expand in the radial direction [Fig. 4(a)]. Because the electric field delays bridge breakup, the contact line on the less wettable surface has more time to retract on that surface. As a result, more liquid is transferred to the more wettable surface when the electric field is present.

B. Leaky dielectrics

We now consider leaky dielectrics where the surface charge density q and liquid conductivity K^* may be nonzero. Note that since conductivity involves charge transport, it brings in an additional timescale.

1. Electrostatic contribution to the tangential stress

For leaky dielectrics, the electric field still makes a contribution to the normal stress balance. However, a nonzero surface charge density and an electric field can also influence the tangential stress balance, as can be seen in Eq. (12). As discussed in Ref. [34] in the context of the 1D model, the transfer ratio can be increased by manipulating the direction of the electrostatic contribution to the tangential stress. The magnitude of this stress is determined by the surface charge density q and the tangential component of the electric field along the interface. The direction of this stress depends on the sign of q and the direction of the electric field since $\chi > 0$.

To enhance liquid transfer to the top plate, the electrostatic contribution to the tangential stress has to be positive so that it points in the positive z-direction. Since the sign of the surface charge may depend on material properties, the direction of the electric field can be adjusted to manipulate the direction of the tangential stress. If the surface charge is negative, then the direction of the electric field should point in the negative z-direction by applying a positive potential on the top plate while grounding the bottom plate (and vice versa; note that $\mathbf{E}_i = -\nabla\phi_i$). The mechanism is illustrated in the schematic shown in Fig. 7.

2. Liquid transfer

We set the initial surface charge density q_o to 0 or 0.5. The latter value of charge density corresponds to 4.4×10^{-6} C/m^2 for a 1 kV potential difference over a 1 mm gap. This initial surface charge density is about two orders of magnitude smaller than the values used in studies of electrospinning [44], but it is large enough to significantly influence bridge behavior. In this section, a constant electrostatic potential is applied at the bottom plate while the top plate is grounded. Therefore, the direction of the electrostatic contribution to the tangential stress is in the positive z-direction.

The second term on the right-hand side of Eq. (5) represents a change in surface charge density due to charge accumulation at the liquid-air interface [39]. We set the dimensionless conductivity K^*

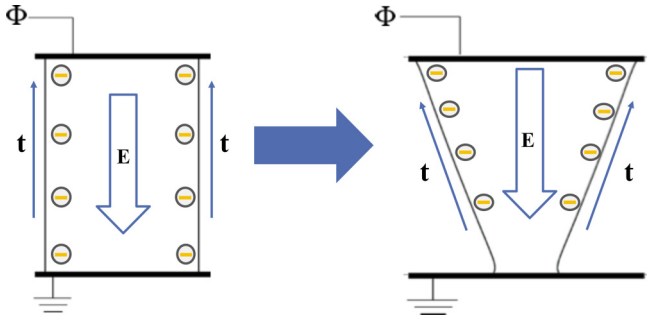

FIG. 7. Schematic illustrating how surface charge and the associated tangential stresses can increase liquid transfer to the top plate. The electric field points in the negative z-direction and the tangential stresses point in the positive z-direction.

to 0 or 1. The latter value corresponds to 8.8×10^{-12} $(\Omega\ \mathrm{m})^{-1}$ for a 1 mm characteristic length and 1 mm/s stretching speed. This conductivity is of the same order of magnitude of what is observed for silicone oil. If K^* is even smaller, not enough surface charge accumulates to significantly influence the bridge shape before the simulation ends.

The diffusion term in Eq. (5) is usually neglected [39], but we keep this term to prevent steep charge gradients that form near each contact line [40]. To determine the value of Pe, we perform some additional calculations using equilibrium bridge shapes (see the Supplemental Material [43] for more details). These calculations indicate that the equilibrium bridge shapes for Pe $\sim$ 1–10^4 are very similar, so we choose a value of Pe $= 1000$ since it provides a reasonable balance between computational accuracy and cost.

To understand how the initial surface charge density and conductivity influence liquid transfer, we consider four different cases: (i) $q_o = 0$, $K^* = 0$ (perfect dielectric); (ii) $q_o = 0.5$, $K^* = 0$; (iii) $q_o = 0$, $K^* = 1$; and (iv) $q_o = 0.5$, $K^* = 1$. Figure 8 shows the transfer ratio for these cases at Ca $= 0.5$, as well as the transfer ratio for the nonelectrified bridge.

In Fig. 8, the values of the transfer ratio for the case in which $q_o = 0$ and $K^* = 1$ are in between the values for the perfect dielectric bridge and the nonelectrified bridge. However, for the case in which $q_o = 0.5$ and $K^* = 0$, the transfer ratio increases about 20% compared to the transfer ratio

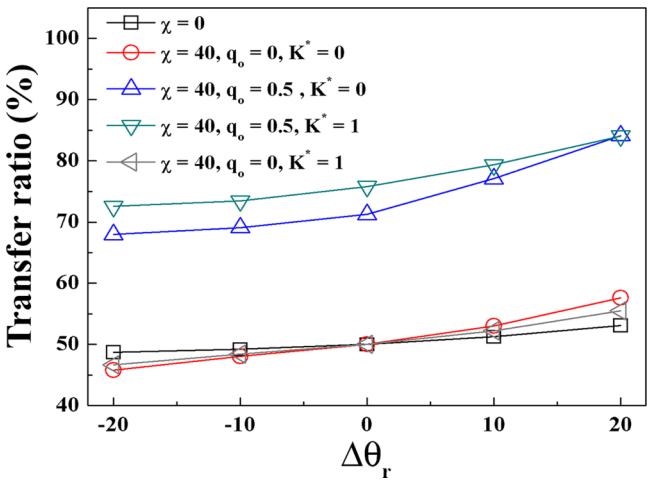

FIG. 8. Transfer ratio vs wettability difference for cases in which $\chi = 0$ (□); $\chi = 40$, $q_o = 0$, $K^* = 0$ (◯); $\chi = 40$, $q_o = 0.5$, $K^* = 0$ (△); $\chi = 40$, $q_o = 0.5$, $K^* = 1$ (▽); and $\chi = 40$, $q_o = 0$, $K^* = 1$ (◁). Here, $\theta_{\mathrm{top}} = 60^\circ$, and θ_{bottom} varies from 40° to 80°. The values of the other parameters are Ca $= 0.5$ and Pe $= 1000$.

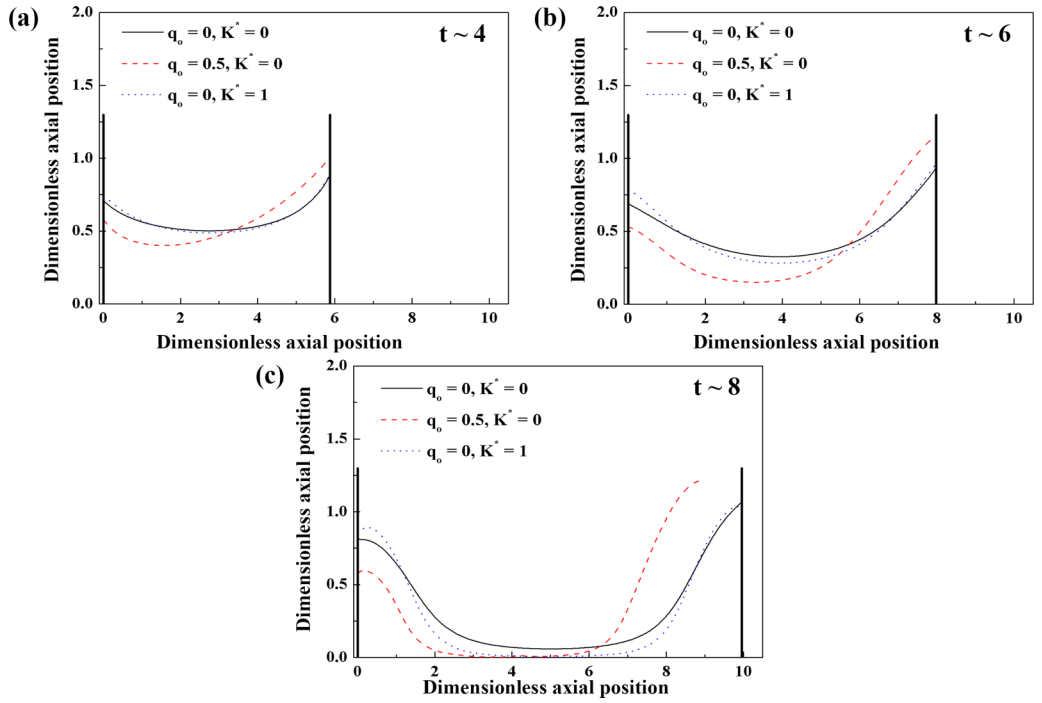

FIG. 9. Bridge shapes at times (a) $t = 4$, (b) $t = 6$, and (c) $t = 8$. The breakup times for the cases with $q_o = 0$, $K^* = 0$ (solid line); $q_o = 0.5$, $K^* = 0$ (dashed line); and $q_o = 0$, $K^* = 1$ (dotted line) are 8.3, 6.9, and 8.0, respectively. The values of the other parameters are Ca $= 0.5$, $\chi = 40$, $\theta_{\text{top}} = 60^\circ$, $\theta_{\text{bottom}} = 80^\circ$, and $\Delta\theta_r = 20^\circ$.

for the perfect dielectric bridge for all values of $\Delta\theta_r$. Additionally, the transfer ratio for the case in which $q_o = 0.5$ and $K^* = 1$ is only about 1–5 % higher than that for the case in which $q_o = 0.5$ and $K^* = 0$.

These results indicate that tangential stresses arising from surface charge can significantly enhance liquid transfer even when the top plate is less wettable than the bottom plate. In addition, they show that the initial surface charge plays a more important role than liquid conductivity in controlling liquid transfer. The predictions of the 2D model are in qualitative agreement with those from the 1D model [34], although the 1D model predicts a higher transfer ratio due to the approximations it makes (see the Supplemental Material [43]).

We now examine bridge shapes at different times to explain why the initial surface charge plays a more important role than conductivity in controlling liquid transfer. Figure 9 shows bridge shapes at several different times. In Fig. 9(a), liquid is pushed to the right (top) plate for the case in which $q_o = 0.5$ and $K^* = 0$, whereas the bridge shapes for the other two cases nearly overlap. As shown in Eq. (12), the electrostatic contribution to the tangential stress is the product of the surface charge and the tangential component of the electric field. Therefore, when the initial surface charge is nonzero, the tangential stress pushes liquid at the beginning of bridge stretching. However, for the case in which $q_o = 0$ and $K^* = 1$, it takes time for charge to accumulate at the liquid-air interface. As a consequence, the tangential stress is not strong enough to significantly influence bridge shape.

At a later time $t = 6$ [Fig. 9(b)], the bridge for the case in which $q_o = 0.5$ and $K^* = 0$ is close to breakup. In addition, the bridge for the case in which $q_o = 0$ and $K^* = 1$ becomes narrower than the bridge for the case in which $q_o = 0$ and $K^* = 0$ due to the presence of tangential stresses. We find that negative surface charge accumulates on the left (bottom) half of the bridge because the left plate is the positive electrode, and vice versa. As a consequence, the tangential stress near the left

plate points in the negative z-direction while the tangential stress near the right plate points in the positive z-direction. This drives liquid to each plate and results in a narrower bridge and a slightly lower transfer ratio (Fig. 8).

Final bridge shapes are shown in Fig. 9(c). The bridge with $q_o = 0.5$ breaks earlier ($t = 6.9$) than the bridges with $q_o = 0$ ($t = 8.0$ for $K^* = 1$ and $t = 8.3$ for $K^* = 0$). These results show that the initial surface charge not only enhances liquid transfer but also reduces the breakup time. However, the breakup time for the bridge with $q_o = 0.5$ is still longer than that for a corresponding nonelectrified bridge [Fig. 4(b)] because of the stabilizing effect of the electric field. If the initial surface charge is zero, the surface charge does not accumulate fast enough for tangential stresses to significantly modify liquid transfer. If the initial surface charge and conductivity are nonzero, the accumulated surface charge can increase the strength of the tangential stress, and the transfer ratio can be further increased (Fig. 8).

IV. RESULTS—CAVITY

In Sec. III, we observed that application of an electric field stabilizes a stretching liquid bridge, which allows more time for the contact line to recede on the less wettable surface and leads to an increase in liquid transfer to the more wettable surface. Tangential stresses due to surface charge can significantly enhance liquid transfer, even to the less wettable surface. Predictions from the 2D model are in qualitative agreement with those of the 1D model presented in our prior work [34]. In this section, we replace the bottom plate with a cavity [Fig. 2(b)] to study how electric fields influence liquid transfer. Because the cavity has a geometry that varies in the radial direction, the 1D model cannot be applied and 2D calculations are necessary.

In our study, the parameters in Eq. (19) are the depth of cavity $\delta = 1$, distance from the symmetry axis to the midpoint of the cavity wall $r_s = 0.8$, and curvature of the corner $r_d = 0.3$; the values chosen are consistent with those used in our previous studies [22,23]. The initial distance between the flat plate and the cavity bottom is 1.2, and consistent with our previous studies [22,23], we begin with a liquid bridge that has a vertical liquid-air interface located 1.05 units away from the symmetry axis. Before stretching the bridge, we run simulations without an electric field with $U = 0$ until the bridge reaches an equilibrium shape. This equilibrium shape is then used as an initial condition when stretching the bridge, both in the absence and presence of an electric field. Since there is already a geometric asymmetry due to the cavity, we use an equilibrium bridge rather than a cylindrical bridge as an initial condition, consistent with our previous work [22,23,25].

A. Perfect dielectrics

1. Effects of electrostatic forces

We begin by examining liquid transfer for perfect dielectrics. The top contact angle θ_{top} is fixed at 70°, while the bottom contact angle θ_{bottom} varies from 50° to 90°. The relative permittivity of the liquid phase is again set to $\epsilon = 2.74$.

Figure 10 shows how the transfer ratio varies as a function of the wettability difference in the absence and presence of an electric field at Ca = 0.1 and 0.5. In Fig. 10(a), where Ca = 0.1, the transfer ratio increases as $\Delta\theta_r$ increases when $\chi = 0$. However, the values of the transfer ratio are much less than those for liquid transfer between two flat plates (Fig. 3). Because the contact line tends to pin on the cavity wall and retract on the flat plate, the resulting droplet that forms on the flat plate is much smaller than that in the cavity [22]. When $\chi = 20$, the transfer ratio increases as $\Delta\theta_r$ increases but does not change much when $\Delta\theta_r < 0°$. However, when χ is further increased to 40, the values of the transfer ratio are larger for all $\Delta\theta_r$ compared to the values when the electric field is absent. The transfer ratio also becomes larger as $\Delta\theta_r$ increases. These results show that if electrostatic forces are strong enough, they can increase liquid transfer from a cavity even when $\Delta\theta_r < 0$.

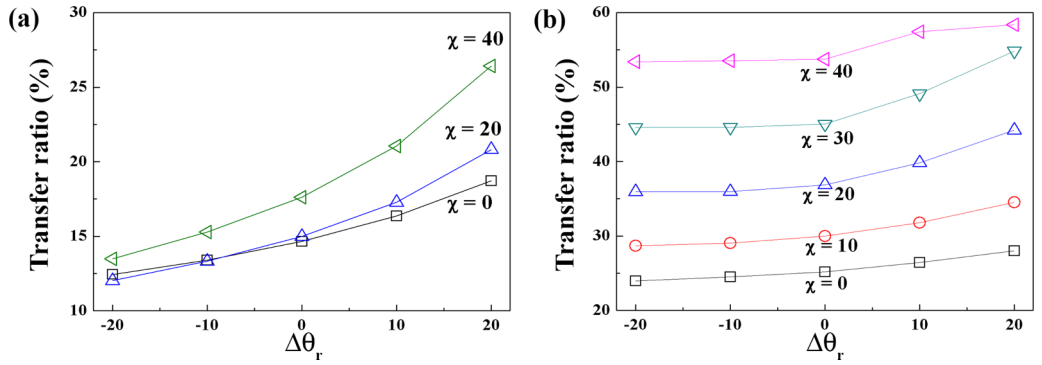

FIG. 10. Relationship between transfer ratio and wettability difference for different values of χ at (a) Ca = 0.1 and (b) Ca = 0.5. Here, $\theta_{\text{top}} = 70^\circ$, and θ_{bottom} varies from 50° to 90°. The wettability difference $\Delta\theta_r = \theta_{\text{bottom}} - \theta_{\text{top}}$.

Comparison of Figs. 10(a) and 10(b) shows that when no electric field is present, the transfer ratio increases as Ca increases from 0.1 to 0.5. Because the viscous forces are stronger at higher Ca, they are more effective at reducing the tendency of the contact line to retract on the flat plate, and as a result, more liquid is transferred there [22]. As can be seen in Fig. 10(b), the transfer ratio increases as χ increases for all $\Delta\theta_r$; the physical mechanisms responsible for this will be discussed below. As noted in Sec. III A 1, the influence of the electric field is more prominent at larger Ca since χCa is larger.

We now characterize how the electric field changes contact-line movement and thus the transfer ratio. Figure 11(a) shows the time evolution of contact-line positions for $\chi = 0$ and 40 at Ca = 0.5 and $\Delta\theta_r = 20^\circ$. In Fig. 11(a), both contact lines slip down each surface at the beginning of stretching for $\chi = 0$. However, the top contact line keeps retracting until bridge breakup, while the bottom contact line effectively pins on the cavity wall [22]. Even though the top plate is more wettable than the cavity, the top contact radius becomes smaller than the bottom contact radius. Therefore, the transfer ratio is only 28% [Fig. 10(b)]. For $\chi = 40$ [Fig. 11(a)], the bottom contact line slips faster than the top contact line. The faster retraction of the bottom contact line down the cavity wall when the electric field is present allows more liquid near the cavity to transfer to the flat plate.

Figure 11(b) shows the final bridge shapes for $\chi = 0$ and 40. In Fig. 11(b), the size of the droplet in the cavity for $\chi = 40$ is smaller than that for $\chi = 0$. Even though the value of the top contact

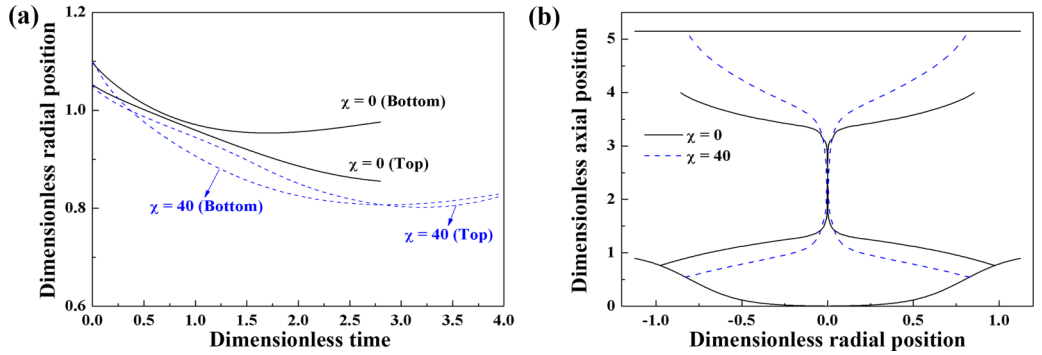

FIG. 11. (a) Time evolution of the contact line on the top (flat plate) and bottom (cavity) surfaces for $\chi = 0$ (solid line) and 40 (dashed line). (b) Final bridge shapes for $\chi = 0$ (solid line) and 40 (dashed line). The bridge breakup times for $\chi = 0$ and 40 are 2.8 and 3.9, respectively. The values of the other parameters are Ca = 0.5, $\theta_{\text{top}} = 70^\circ$, $\theta_{\text{bottom}} = 90^\circ$, and $\Delta\theta_r = 20^\circ$.

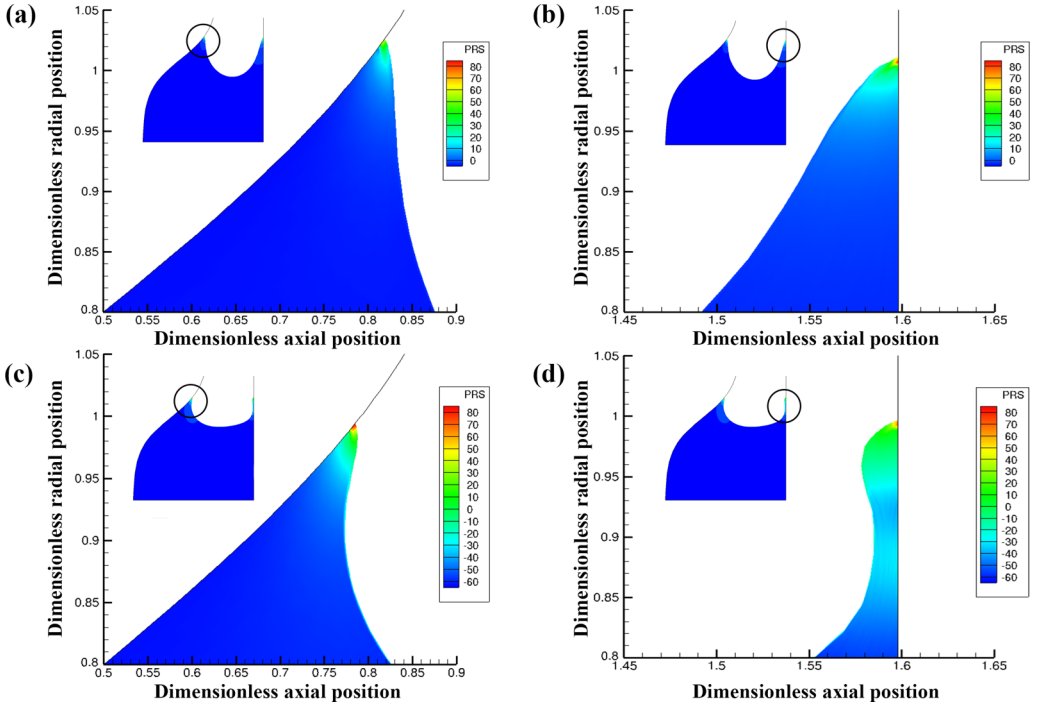

FIG. 12. Pressure contours and interface shapes for (a), (b) $\chi = 0$ and (c), (d) $\chi = 40$ at $t = 0.4$. Panels (a) and (c) show the region near the contact line on the cavity wall, and panels (b) and (d) show the region near the flat plate. The values of the other parameters are Ca $= 0.5$, $\theta_{\text{top}} = 70^\circ$, $\theta_{\text{bottom}} = 90^\circ$, and $\Delta\theta_r = 20^\circ$. The insets show the locations of the interface shapes.

radius for $\chi = 40$ is slightly smaller than that for $\chi = 0$ [Fig. 11(a)], the size of the top droplet for the electrified bridge is larger than that for the nonelectrified bridge [Fig. 11(b)]. These results show that the electric field enhances liquid transfer by increasing contact-line slippage on the cavity wall, thus pushing more liquid to the top plate. Note that the electrified bridge breaks up at a longer length than the nonelectrified bridge because the electric field stabilizes the bridge as discussed in Sec. III A 2.

To understand how the electric field promotes contact-line movement on the cavity wall, it is useful to analyze pressure contours near the contact lines as shown in Fig. 12. Figures 12(a) and 12(b) show pressure contours for $\chi = 0$ at $t = 0.4$. At the right (top) surface [Fig. 12(b)], the highest pressure is near the contact line, and the pressure decreases away from the contact line. Such a pressure gradient drives liquid away from the contact line, causing it to retract. At the left (bottom) contact line [Fig. 12(a)], the pressure gradient is smaller than that near the right (top) contact line. As discussed in Ref. [22], the interface near the cavity wall does not have to deform as much to maintain a constant contact angle due to the inclination of the cavity wall. As a consequence, the capillary pressure gradients there are smaller compared to those near the contact line on the flat plate, and the contact line effectively pins on the cavity wall (Fig. 11).

Figures 12(c) and 12(d) show pressure contours for $\chi = 40$ at $t = 0.4$. As discussed in Sec. III A 2, the presence of the electric field decreases the pressure near the bridge center. Figures 12(c) and 12(d) show that the lowest pressure for the electrified bridge is much smaller than that for the nonelectrified bridge [Figs. 12(a) and 12(b)]. As a result, there is a higher pressure gradient near the contact line on the right (top) surface [Fig. 12(d)] compared to the case in which $\chi = 0$ [Fig. 12(b)]. The higher pressure gradient drives more liquid away from the contact line,

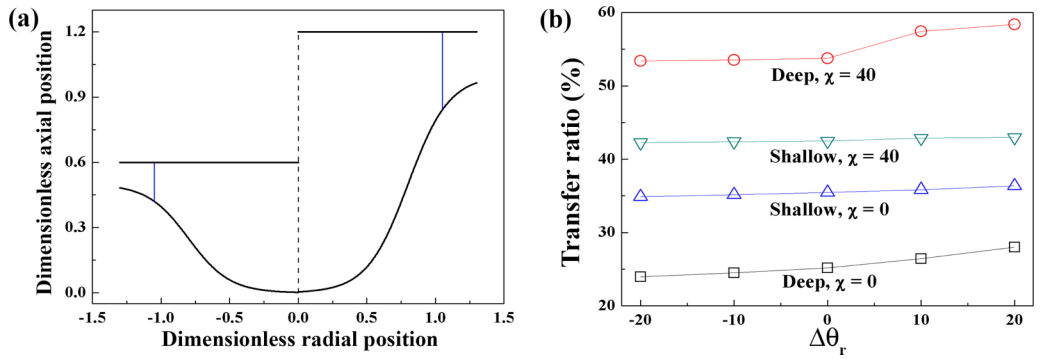

FIG. 13. (a) Cavity shapes for $\delta = 1$ (right) and 0.5 (left). (b) Relationship between transfer ratio and wettability difference for different values of χ and cavity depths at Ca = 0.5. Here, $\theta_{\text{top}} = 70^\circ$, and θ_{bottom} varies from 50° to 90°.

leading to a large change in interface shape. In particular, a thin film of liquid forms on the top plate.

At the left (bottom) surface, the maximum pressure near the contact line is increased when the electric field is present [Figs. 12(c) and 12(a)]. This, along with a lower pressure near the bridge center, leads to a higher pressure gradient near the contact line on the cavity wall, causing it to slip more. This overcomes the apparent pinning that was observed in the absence of the electric field (Fig. 11), and it allows more liquid to be transferred to the top plate. We also observe that the interface is more highly curved near the cavity wall and begins to form a thin film when the electric field is present. Although the contact line on the top plate retracts more when the electric field is present, the increased slippage of the contact line on the cavity wall outweighs this effect and leads to an increase in the transfer ratio.

2. Effect of cavity depth

In this section, we report results from a brief parametric study examining the influence of cavity depth on liquid transfer. Here, the depth of cavity $\delta = 0.5$, which is one-half the value used in the previous section; the rest of the parameters in Eq. (19) remain the same. Figure 13(a) shows the two cavity shapes. Because we use a hyperbolic tangent function to define cavity shape, the angle between the cavity bottom and the cavity wall increases about 7° when δ decreases from 1 to 0.5. The depth is decreased by 50% while the angle is changed only about 6%, so any change in the transfer ratio is likely mainly due to the change in cavity depth. The initial distance between the flat plate and the cavity for the shallower cavity is taken to be 0.6; this is half the value used in the previous section, and it was chosen since the cavity depth has been halved.

Figure 13(b) shows the transfer ratio for the two cavity depths at Ca = 0.5. When $\chi = 0$, the transfer ratio for the shallow cavity is higher than that for the deep cavity because the contact line on the shallow cavity slips more (results not shown). This result can be rationalized by noting that the cavity becomes a flat plate when δ approaches 0. Note that the transfer ratio for the geometry having two flat plates with $\Delta\theta_r = 20^\circ$ and Ca = 0.5 is approximately 50%. Therefore, the transfer ratio increases as the cavity becomes shallower.

When $\chi = 40$, the transfer ratio increases relative to the $\chi = 0$ case for both the deep and shallow cavities for all wettability differences. Notably, the transfer ratio for the deep cavity increases about 30% while the transfer ratio for the shallow cavity only increases about 8%. Thus, the deep cavity eventually transfers more liquid to the top plate than the shallow cavity when the electric field is applied, which is the opposite to what is observed when the electric field is absent.

We now discuss the reason why the deep cavity transfers more liquid than the shallow cavity when the electric field is present. Figure 14 shows pressure contours for the shallow and deep cavity

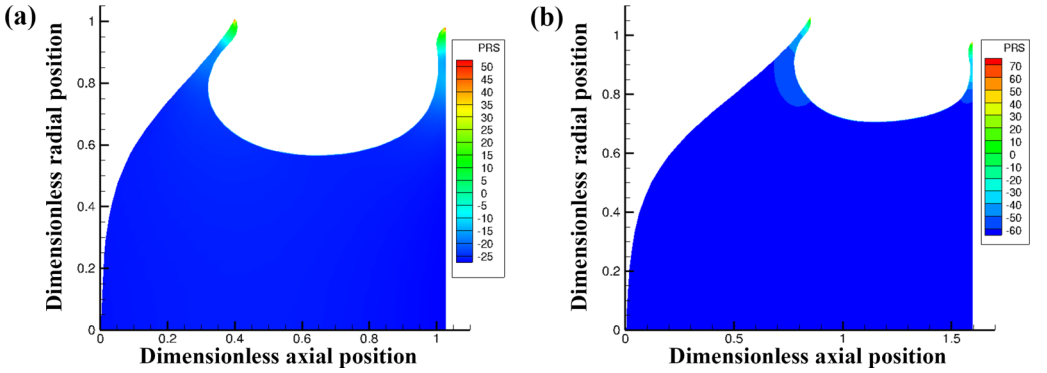

FIG. 14. Pressure contours and interface shapes for (a) the shallow cavity and (b) the deep cavity at $t = 0.4$. Values of other parameters are Ca $= 0.5$, $\chi = 40$, $\theta_{\text{top}} = 70^\circ$, $\theta_{\text{bottom}} = 90^\circ$, and $\Delta\theta_r = 20^\circ$.

at $t = 0.4$. In both cases, the pressure is uniform over much of the domain, but large pressure gradients arise near the contact lines.

For the shallow cavity [Fig. 14(a)], the dimensionless pressure difference between the vicinity of cavity wall and bulk is about 75. For the deep cavity [Fig. 14(b)], the dimensionless pressure difference is about 150. This higher pressure difference arises from the change in curvature near the contact line at the cavity wall. For the shallow cavity, the curvature near the contact line does not need to vary as much to maintain a contact angle. Therefore, the pressure difference in the shallow cavity is smaller than that of the deep cavity. At the later times (results not shown), the curvature of the interface in the shallow cavity becomes nearly constant, which causes the contact line to effectively pin. However, the interface of the deep cavity remains highly curved until the end of the stretching. Consequently, for the deep cavity, the capillary pressure gradient pumps liquid away from the cavity wall, causing the transfer ratio to increase.

In summary, by modifying the pressure distribution in the liquid bridge, the electric field also modifies the interface shapes and pressure gradients near the contact lines. This modification is more pronounced for the deep cavity, and it results in a larger transfer ratio compared to the shallow cavity.

B. Leaky dielectrics

In Sec. III B, we found that tangential stresses due to surface charge have a significant influence on liquid transfer when both plates are flat. We now study the impact of the initial surface charge and conductivity on liquid transfer when the bottom plate is replaced by a cavity. We consider the cases in which (i) $q_o = 0$, $K^* = 0$ (perfect dielectric); (ii) $q_o = 0.5$, $K^* = 0$; (iii) $q_o = 0$, $K^* = 1$; and (iv) $q_o = 0.5$, $K^* = 1$. The initial shapes and contact angles are the same as those used in Sec. IV A 1. The electroviscous number $\chi = 40$, and the capillary number Ca $= 0.5$. As in Sec. III B, a constant electrostatic potential is applied at the bottom plate while the top plate is grounded so that the electrostatic contribution to the tangential stress tends to point in the positive z-direction.

Figure 15(a) shows the transfer ratio for perfect dielectrics ($q_o = 0$, $K^* = 0$) and leaky dielectrics at Ca $= 0.5$ and $\chi = 40$. The values of the transfer ratio for the leaky dielectric cases are about 2% higher or lower than those for the perfect dielectric.

Figure 15(b) shows the final bridge shapes for these four cases when $\theta_{\text{top}} = \theta_{\text{bottom}} = 70^\circ$. The final shapes almost overlap except for the region near the right (top) plate, and the bridge breakup times are all within 5% of the prefect-dielectric value. In contrast to the case in which both surfaces are flat (Fig. 9), the electrostatic contribution to the tangential stress does not appear to significantly influence the movement of the contact line on the left (bottom) surface. In addition, the behavior of the transfer ratio and breakup times with respect to q_0 and K^* is less systematic than what is observed

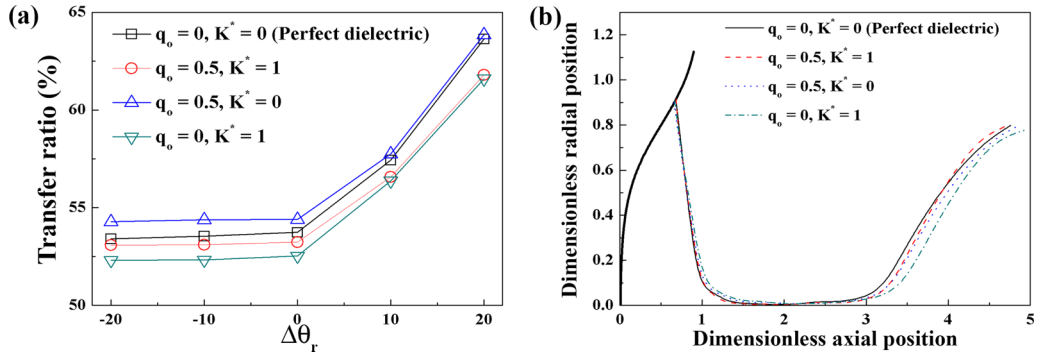

FIG. 15. (a) Relationship between transfer ratio and wettability difference when (i) $q_o = 0$, $K^* = 0$ (□); (ii) $q_o = 0.5$, $K^* = 0$ (△); (iii) $q_o = 0$, $K^* = 1$ (▽); and (iv) $q_o = 0.5$, $K^* = 1$ (◯). Here, $\theta_{\text{top}} = 70°$, and θ_{bottom} varies from 50° to 90°. (b) Final bridge shapes for different cases when $\theta_{\text{top}} = \theta_{\text{bottom}} = 70°$. The bridge breakup times for cases (i)–(iv) are 3.56, 3.64, 3.73, and 3.55, respectively. Values of other parameters are Ca = 0.5 and $\chi = 40$.

for liquid transfer between two flat plates (Fig. 8). These results indicate that the electrostatic contribution to the tangential stress has a much smaller effect on liquid transfer when the bottom plate is replaced by a cavity. We have performed some additional calculations with $q_o = 1$ and 5 (results not shown), but the increase in the transfer ratio is still less than 5%.

From Eq. (12), the magnitude of the tangential stress is determined by the tangential component of the electric field and the surface charge density. To gain some insight into the results shown in Fig. 15, we compare the electrostatic potential for liquid transfer between two flat plates and liquid transfer between a flat plate and a cavity. We choose the case in which $q_o = 0.5$ and $K^* = 1$, and to exclude the influence of wettability differences, we set $\theta_{\text{top}} = \theta_{\text{bottom}} = 70°$.

Figure 16(a) shows the electrostatic potential contours for the case with two flat plates at $t = 0.6$. Figure 16(c) shows the corresponding tangential component of the electric field, surface charge, and electrostatic contribution to the tangential stress as a function of the arc-length coordinate along the interface. Since $\mathbf{E} = -\nabla\psi$, the direction of the electric field is from left to right. In Fig. 16(a), the bridge interface is nearly parallel to the electric field. In addition, because the slope of the interface near each contact line is higher than that near the center of the bridge, the tangential component of the electric field near the center is greater than that near each contact line [Fig. 16(c)]. As can be seen in Fig. 16(c), the surface charge is still uniformly distributed except near each contact line. The surface charge is approximately zero near the left surface, and it is positive near the right surface because the flow of liquid at the interface is from left to right. As a result, the tangential stress pushes liquid to the right surface and enhances liquid transfer.

Figure 16(b) shows the electrostatic potential contours for the case with the cavity at $t = 0.6$. Figure 16(d) shows the corresponding tangential component of the electric field, surface charge, and electrostatic contribution of the tangential stress along the interface. In Fig. 16(b), the interface near each contact line is highly curved and nearly perpendicular to the direction of the electric field (positive z-direction). Therefore, as can be seen in Fig. 16(d), the tangential component of the electric field varies considerably near each contact line and is close to zero in some places. Near the center of the bridge, the tangential component of the electric field is relatively uniform. The surface charge is negative near the left contact line, and it increases to positive values as the right contact line is approached. The resulting tangential stresses over much of the bridge length are positive, but near each contact line they are close to zero and even negative. The positive tangential stresses tend to drive liquid to the right. However, the near-zero and negative tangential stresses near the contact lines lead to little additional contact line movement. Moreover, the thin films of liquid that form near each contact line provide additional viscous resistance to the tangential stresses. These factors

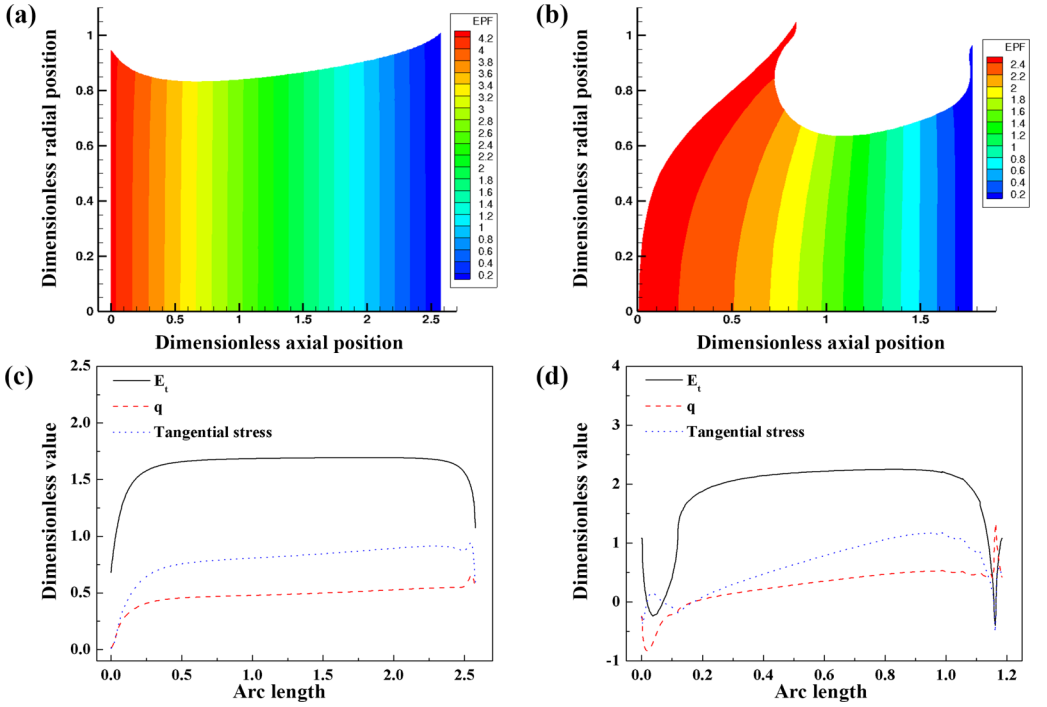

FIG. 16. (a), (b) Electrostatic potential contours and (c), (d) electrostatic contribution to the tangential stress for liquid transfer between (a), (c) flat plates and (b), (d) a flat plate and a cavity at $t = 0.6$. The values of the other parameters are Ca $= 0.5$, $\chi = 40$, $\theta_{\text{top}} = \theta_{\text{bottom}} = 70^\circ$, $q_o = 0.5$, and $K^* = 1$.

may account for the less systematic behavior of the behavior of the transfer ratio and breakup times with respect to q_0 and K^* (Fig. 15).

V. CONCLUSIONS

Motivated by the use of electrostatic assist to improve liquid transfer in printing processes, we have examined the influence of electric fields on liquid transfer in two model geometries, both of which involve liquid bridges with moving contact lines. For liquid transfer between two flat plates, application of an electric field stabilizes the liquid bridge. This allows more time for the contact line to retract on the less wettable surface, and it leads to an increase in liquid transfer to the more wettable surface. Tangential stresses due to surface charge can significantly enhance liquid transfer, even to the less wettable surface if the tangential stresses point toward that surface. The initial surface charge plays a more important role than liquid conductivity in enhancing liquid transfer. Predictions from the 2D model used in this work are in qualitative agreement with those of the 1D model presented in our prior work.

For liquid transfer between a flat plate and a cavity, the electric field modifies the pressure distribution in the bridge, and as a consequence, also the interface shapes and pressure gradients near the contact lines. In particular, the pressure gradient near the contact line on the cavity wall is increased, causing the contact line to slip more. This overcomes the apparent pinning that occurs in the absence of the electric field, and it allows more liquid to be transferred to the top plate, even when the top plate is less wettable than the cavity. Notably, the modification is more pronounced for a deep cavity, resulting in a larger transfer ratio compared to a shallow cavity. In contrast to the case of liquid transfer between two flat plates, surface charge does not have as significant an influence

on liquid transfer due to the way the cavity and electric field modify the interface shape near the contact line.

The results of this work provide a foundation for understanding the physical mechanisms underlying electrostatic assist. At high printing speeds (Ca $\sim$ 1), the transfer ratio is only 50% in the absence of an electric field for liquid transfer between two flat plates. For liquid transfer from a cavity, the transfer ratio can be even lower due to an apparent pinning of the contact line on the cavity wall. To overcome these limits, and thus reduce printing defects, additional forces such as electric fields must be used.

The present work illustrates the physical mechanisms through which electric fields can improve liquid transfer. The results provide a foundation for additional studies that incorporate shear and rotational motion, multiple cavities, and non-Newtonian rheology. They also highlight the need for complementary experiments, especially those that can test the predictions reported here. The results of such investigations are relevant not only to printing, but potentially also to other applications [11] such as adhesion, tribology, and microfluidics, where liquid bridges with moving contact lines appear.

ACKNOWLEDGMENTS

This work was supported through the Industrial Partnership for Research in Interfacial and Materials Engineering of the University of Minnesota. We are grateful to the Minnesota Supercomputing Institute (MSI) at the University of Minnesota for providing computational resources.

[1] B. Kang, W. H. Lee, and K. Cho, Recent advances in organic transistor printing processes, Appl. Mater. Interf. **5**, 2302 (2013).

[2] P. F. Moonen, I. Yakimets, and J. Huskens, Fabrication of transistors on flexible substrates: From mass-printing to high-resolution alternative lithography strategies, Adv. Mater. **24**, 5526 (2012).

[3] H. Kang, R. Kitsomboonloha, K. Ulmer, L. Stecker, G. Grau, J. Jang, and V. Subramanian, Megahertz-class printed high mobility organic thin-film transistors and inverters on plastic using attoliter-scale high-speed gravure-printed sub-5 μm gate electrodes, Org. Electron. **15**, 3639 (2014).

[4] F. C. Krebs, Fabrication and processing of polymer solar cells: A review of printing and coating techniques, Sol. Energy Mater. Sol. Cells **93**, 394 (2009).

[5] M. Jung, J. Kim, J. Noh, N. Lim, C. Lim, G. Lee, K. Kim, H. Kang, K. Jung, A. D. Leonard, J. M. Tour, and G. Cho, All-printed and roll-to-roll-printable 13.56-MHz-operated 1-bit RF tag on plastic foils, IEEE Trans. Electron Dev. **57**, 571 (2010).

[6] Y. Zheng, Z. He, Y. Gao, and J. Liu, Direct desktop printed-circuits-on-paper flexible electronics, Sci. Rep. **3**, 1786 (2013).

[7] S. Khan, L. Lorenzelli, and R. S. Dahiya, Technologies for printing sensors and electronics over large flexible substrates: A review, IEEE Sens. J. **15**, 3164 (2015).

[8] Q. Thiburce and A. J. Campbell, Low-voltage polyelectrolyte-gated polymer field-effect transistors gravure printed at high speed on flexible plastic substrates, Adv. Electron. Mater. **3**, 1600421 (2016).

[9] D. Tobjork and R. Osterbacka, Paper Electron., Adv. Mater. **23**, 1935 (2011).

[10] D. Sung, A. F. Vornbrock, and V. Subramanian, Scaling and optimization of gravure-printed silver nanoparticle lines for printed electronics, IEEE Trans. Compon. Packag. Technol. **33**, 105 (2010).

[11] S. Kumar, Liquid transfer in printing processes: Liquid bridges with moving contact lines, Annu. Rev. Fluid Mech. **47**, 67 (2015).

[12] G. Grau, J. Cen, H. Kang, R. Kitsomboonloha, W. J. Scheideler, and V. Subramanian, Gravure-printed electronics: Recent progress in tooling development, understanding of printing physics, and realization of printed devices, Flex. Print. Electron **1**, 023002 (2016).

[13] A. V. Joshi, C. Dettke, and J. Steingraeber, Investigation on electrostatic assist and gravure process parameters on solid mottle reduction for shrink films, J. Coat. Technol. Res. **13**, 375 (2016).
[14] A. Ramkrishnan and S. Kumar, Electrohydrodynamic deformation of thin liquid films near surfaces with topography, Phys. Fluids **26**, 122110 (2014).
[15] H. F. George, Electrostatically assisted ink transfer in gravure printing, ACS Symp. Ser. **200**, 359 (1982).
[16] K. Morris, Electrostatically assisted gravure, Print. Technol. **12**, 180 (1968).
[17] S. Dodds, M. S. Carvalho, and S. Kumar, The dynamics of three-dimensional liquid bridges with pinned and moving contact lines, J. Fluid Mech. **707**, 521 (2012).
[18] X. Yin and S. Kumar, Flow visualization of the liquid-emptying process in scaled-up gravure grooves and cells, Chem. Eng. Sci. **61**, 1146 (2006).
[19] H. Chen, T. Tang, and A. Amirfazli, Liquid transfer mechanism between two surfaces and the role of contact angles, Soft Matter **10**, 2503 (2014).
[20] H. Chen, T. Tang, and A. Amirfazli, Effects of surface wettability on fast liquid transfer, Phys. Fluids **27**, 112102 (2015).
[21] H. Chen, T. Tang, and A. Amirfazli, Fast liquid transfer between surfaces: Breakup of stretched liquid bridges, Langmuir **31**, 11470 (2015).
[22] S. Dodds, M. S. Carvalho, and S. Kumar, Stretching and slipping of liquid bridges near plates and cavities, Phys. Fluids **21**, 092103 (2009).
[23] S. Dodds, M. S. Carvalho, and S. Kumar, Stretching liquid bridges with moving contact lines: The role of inertia, Phys. Fluids **23**, 092101 (2011).
[24] C.-H. Huang, M. S. Carvalho, and S. Kumar, Stretching liquid bridge with moving contact lines: Comparison of liquid-transfer predictions and experiments, Soft Matter **12**, 7457 (2016).
[25] J.-T. Wu, M. S. Carvalho, and S. Kumar, Transfer of rate-thinning and rate-thickening liquids between separating plates and cavities, J. Non-Newtonian Fluid Mech. **255**, 57 (2018).
[26] A. K. Sankaran and J. P. Rothstein, Effect of viscoelasticity on liquid transfer during gravure printing, J. Non-Newtonian Fluid Mech. **175–176**, 64 (2012).
[27] D. M. Campana and M. S. Carvalho, Liquid transfer from single cavities to rotating rolls, J. Fluid Mech. **747**, 545 (2014).
[28] D. M. Campana, S. Ubal, M. D. Giavedoni, F. A. Saita, and M. S. Carvalho, Three dimensional flow of liquid transfer between a cavity and a moving roll, Chem. Eng. Sci. **149**, 169 (2016).
[29] J. A. Lee, J. P. Rothstein, and M. Pasquali, Computational study of viscoelastic effects on liquid transfer during gravure printing, J. Non-Newtonian Fluid Mech. **199**, 1 (2013).
[30] C. L. Burcham and D. A. Saville, The electrohydrodynamic stability of a liquid bridge: Microgravity experiments on a bridge suspended in a dielectric gas, J. Fluid Mech. **405**, 37 (2000).
[31] C. L. Burcham and D. A. Saville, Electrohydrodynamic stability: Taylor-Melcher theory for a liquid bridge suspended in a dielectric gas, J. Fluid Mech. **452**, 163 (2002).
[32] S. Sankaran and D. A. Saville, Experiments on the stability of a liquid bridge in an axial electric field, Phys. Fluids **5**, 1081 (1993).
[33] A. Ramos, H. Gonzalez, and A. Castellanos, Experiments on dielectric liquid bridges subjected to axial electric fields, Phys. Fluids **6**, 3206 (1994).
[34] C.-H. Huang and S. Kumar, Electrostatic assist of liquid transfer between flat surfaces, Langmuir **34**, 5124 (2018).
[35] T. D. Blake, The physics of moving wetting lines, J. Colloid Interface Sci. **299**, 1 (2006).
[36] J. B. Bostwick and P. H. Steen, Stability of constrained capillary surfaces, Annu. Rev. Fluid Mech. **47**, 539 (2015).
[37] G. Taylor, Studies in electrohydrodynamics. I. The circulation produced in a drop by an electric field, Proc. R. Soc. London, Ser. A **291**, 159 (1966).
[38] J. R. Melcher and G. I. Taylor, Electrohydrodynamics: A review of the role of interfacial shear stresses, Annu. Rev. Fluid Mech. **1**, 111 (1969).
[39] D. A. Saville, Electrohydrodynamics: The Taylor-Melcher leaky dielectric model, Annu. Rev. Fluid Mech. **29**, 27 (1997).

[40] A. Corbett and S. Kumar, Spreading of thin droplets of perfect and leaky dielectric liquids on inclined surfaces, Langmuir **32**, 6606 (2016).

[41] A. Ramkrishnan and S. Kumar, Electrohydrodynamic effects in the leveling of coatings, Chem. Eng. Sci. **101**, 785 (2013).

[42] P. M. Gresho, R. L. Lee, and R. L. Sani, On the time-dependent solution of the incompressible Navier-Stokes equations in two and three dimensions, in *Recent Advances in Numerical Methods in Fluids*, edited by C. Taylor and K. Morgan (Pineridge, Swansea, 1980), p. 2779.

[43] See Supplemental Material at http://link.aps.org/supplemental/10.1103/PhysRevFluids.4.044005 for discussions of the 1D model and charge diffusion.

[44] J. J. Feng, The stretching of an electrified non-Newtonian jet: A model for electrospinning, Phys. Fluids **14**, 3912 (2002).